

MambaFusion: Adaptive State-Space Fusion for Multimodal 3D Object Detection

Venkatraman Narayanan Bala Sai Rahul Ahuja Pratik Likhari
Varun Ravi Kumar Senthil Yogamani

Qualcomm Inc.

Abstract

*Reliable 3D object detection is fundamental to autonomous driving, and multimodal fusion algorithms using cameras and LiDAR remain a persistent challenge. Cameras provide dense visual cues but ill posed depth; LiDAR provides a precise 3D structure but sparse coverage. Existing BEV-based fusion frameworks have made good progress, but they have difficulties including inefficient context modeling, spatially invariant fusion, and reasoning under uncertainty. We introduce **MambaFusion**, a unified multimodal detection framework that achieves efficient, adaptive, and physically grounded 3D perception. MambaFusion interleaves selective state-space models (SSMs) with windowed transformers to propagate the global context in linear time while preserving local geometric fidelity. A multi-modal token alignment (MTA) module and reliability-aware fusion gates dynamically re-weight camera–LiDAR features based on spatial confidence and calibration consistency. Finally, a structure-conditioned diffusion head integrates graph-based reasoning with uncertainty-aware denoising, enforcing physical plausibility, and calibrated confidence. MambaFusion establishes new state-of-the-art performance on nuScenes benchmarks while operating with linear-time complexity. The framework demonstrates that coupling SSM-based efficiency with reliability-driven fusion yields robust, temporally stable, and interpretable 3D perception for real-world autonomous driving systems.*

1. Introduction

Robust 3D object detection is the cornerstone of autonomous perception. Cameras capture rich semantics but are unreliable for depth; LiDAR provides precise geometry yet remains sparse and costly. Achieving reliable perception, therefore, hinges on *how effectively these modalities are fused* into a unified spatial understanding of the scene.

Recent bird’s-eye-view (BEV) frameworks [2, 28, 34, 51] have transformed multi-sensor fusion by projecting het-

erogeneous features into a common geometric space. However, despite steady progress, four long-standing challenges continue to limit performance. (1) **Inefficient context modeling**: transformer-based 3D encoders offer global awareness but scale quadratically, making long-range and temporal reasoning computationally expensive. (2) **Spatially invariant fusion**: most systems fuse modalities with fixed or global weights, ignoring that sensor reliability varies with distance, occlusion, and calibration drift. (3) **Lack of physical reasoning**: current detectors predict object confidence purely from feature activations, without enforcing geometric plausibility or structural consistency. (4) **Temporal instability**: detections often fluctuate across frames due to the absence of cross-time feature constraints.

We introduce **MambaFusion**, a unified, end-to-end architecture that bridges these gaps through efficient state-space modeling, adaptive reliability-aware fusion, and structure-conditioned reasoning. First, a *hybrid LiDAR encoder* interleaves Mamba state-space blocks with windowed attention, enabling linear-time propagation of global context while preserving fine local geometry. Second, an *adaptive multi-modal fusion decoder* aligns camera and LiDAR features via a learnable token alignment (MTA) module, followed by spatial reliability gates that dynamically adjust sensor contributions based on point density, multi-view consistency, and projection confidence. Third, a *structure-conditioned diffusion head* refines detections through graph-based reasoning and uncertainty-guided denoising, enforcing physical plausibility and calibrated confidence. Finally, a temporal self-distillation objective stabilizes features across frames, yielding temporally consistent and trustworthy perception.

Our contributions are summarized as follows:

- **Hybrid linear-time LiDAR encoder**: interleaving Mamba state-space blocks and windowed transformers achieves efficient global-local modeling without quadratic attention overhead.
- **Adaptive reliability-aware fusion**: a learnable alignment and gating mechanism dynamically reweights cam-

era–LiDAR features based on spatial confidence and sensor reliability.

- **Structure-conditioned diffusion refinement:** integrates graph reasoning and diffusion-based denoising to enforce geometric plausibility and calibrated uncertainty.
- **Unified, temporally stable perception:** MambaFusion delivers state-of-the-art performance on nuScenes dataset with superior robustness to calibration noise, sparsity, and dynamic scenes.

MambaFusion demonstrates that coupling selective state-space models with reliability-driven fusion yields an efficient, interpretable, and physically grounded approach to multi-sensor 3D perception.

2. Related Work

2.1. Camera-based 3D Object Detection

Camera-only 3D detection methods typically transform multi-view features into bird’s-eye-view (BEV) representations, enabling spatial reasoning. Lift–Splat–Shoot (LSS) [38] first predicted per-pixel depth distributions to lift image features into BEV space. BEVDet [15] and BEVDepth [25] improved geometric accuracy through explicit depth supervision, while temporal extensions such as BEVDet4D [16] and SOLOFusion [37] exploited temporal aggregation for motion understanding. Query-based approaches (e.g., DETR3D [47], PETR [31]) introduced learnable 3D queries projected into image space for end-to-end detection. BEVFormer [29] unified these ideas with deformable spatial cross-attention and temporal transformers, setting the foundation for camera-based BEV feature extraction. Our work adopts BEVFormer’s multi-view encoder but replaces quadratic temporal attention with a linear-time state-space model to improve scalability.

2.2. LiDAR-based 3D Object Detection

LiDAR sensors provide explicit geometry but remain computationally expensive. VoxelNet [60] pioneered voxel-based encoding; SECOND [53] introduced sparse 3D convolutions for efficiency; and CenterPoint [56] popularized center-based detection. Recent transformer-based backbones, such as VoTr [36] and DSVT [46], have improved global context modeling but suffer from quadratic complexity with respect to voxel count. This motivates the need for alternative sequence models that can retain global awareness while scaling linearly with scene size—a capability our Mamba-based LiDAR encoder provides.

2.3. Efficient Sequence Models for Vision

State-space models (SSMs) have recently emerged as efficient alternatives to traditional models, such as transformers. Mamba [12] introduced selective SSMs that achieve input-dependent long-range modeling with linear complex-

ity, inspiring variants in vision tasks [32, 61]. PointMamba [30] and PointSSM [58] extended this idea to point clouds, demonstrating that SSMs can capture geometric continuity effectively. Hybrid designs [14] that interleave SSMs for global propagation with local attention for detailed reasoning show strong potential for structured data. MambaFusion builds directly on this paradigm, alternating SSM and windowed attention blocks to jointly model long-range temporal dependencies and local 3D structure.

2.4. Windowed Attention Mechanisms

Windowed attention reduces the quadratic cost of global transformers while preserving spatial locality. Swin Transformer [33] introduced shifted windows for efficient image modeling, later extended to 3D through stratified or sliding-window designs [21, 44]. In MambaFusion, windowed attention complements SSM propagation by refining local geometry and ensuring accurate spatial alignment in BEV space.

2.5. Multi-Modal Fusion for 3D Detection

Integrating complementary sensors remains a significant challenge in autonomous perception. Early fusion methods (PointPainting [45], MVX-Net [41]) combined image semantics with LiDAR points directly, while BEV-space fusion later emerged as the dominant approach. BEVFusion [35] unified camera and LiDAR features in a shared BEV plane, TransFusion [1] used transformer decoders for soft association, and CMT [52] simplified fusion through token interaction. However, these methods typically apply fixed or globally shared fusion weights, thereby ignoring spatially varying reliability and calibration drift. Our **Multi-Modal Token Alignment (MTA)** explicitly corrects calibration offsets. At the same time, the adaptive fusion gate dynamically modulates sensor contribution based on reliability signals such as point density and cross-view consistency.

2.6. Uncertainty and Calibration in Perception

Accurate confidence estimation is essential for robust fusion. Aleatoric and epistemic uncertainty modeling [20] improves reliability, and evidential regularization [39] encourages calibrated predictions. In multi-sensor systems, spatial misalignment and synchronization errors degrade fusion performance. Recent works address this issue through pose correction or probabilistic alignment. MambaFusion integrates uncertainty-aware weighting directly into the fusion process, using inverse-variance fusion to downweight unreliable regions and ensure stable multi-modal aggregation.

2.7. Spatial Reasoning and Diffusion-based Refinement

Spatial context helps resolve ambiguous detections. Graph-based reasoning, as in PointGNN [40], models object relationships for consistency, while diffusion-based detectors [5, 7] formulate detection as iterative denoising for confidence refinement. We unify these ideas by coupling graph-based spatial reasoning with a **structure-conditioned diffusion module** that refines proposal confidences under geometric and contextual guidance. This combination enables both physically plausible detections and calibrated confidence estimation.

3. Methodology

We propose **MambaFusion**, a unified, end-to-end framework for multi-modal 3D object detection that addresses three core challenges in sensor fusion: (i) efficiently encoding long-range and fine-grained structure in sparse 3D data, (ii) dynamically weighting sensor contributions according to spatial reliability and contextual cues, and (iii) explicitly modeling physical plausibility and uncertainty in detection outcomes. Existing fusion methods [1, 35, 52, 54] typically employ spatially uniform fusion or deterministic weighting, limiting robustness to miscalibration, sparsity, and ambiguous object geometry. An overview of the whole pipeline is illustrated in Fig. 1.

3.1. Multi-Scale Hybrid LiDAR Encoding

Sparse convolutions offer efficiency but limited receptive fields, while pure attention achieves global context at quadratic cost. We resolve this trade-off via a hybrid LiDAR encoder that alternates **Mamba State-Space Model (SSM)** blocks [13, 30] for global context propagation and **windowed Transformers** [33] for local spatial reasoning. Raw LiDAR points are voxelized, serialized along a Hilbert space-filling curve to preserve spatial adjacency, and processed through multiple spatial scales with alternating SSM and attention blocks. SSM layers model long-range dependencies in linear time, while windowed attention captures fine structural detail. Cross-scale aggregation and residual links generate multi-scale BEV features that balance global awareness and local precision. We denote the resulting LiDAR BEV representation as Q_L^{BEV} .

3.2. Spatiotemporal Camera BEV Aggregation

Multi-view images are encoded using a shared backbone with feature pyramid network (FPN) features. Following [29], learnable BEV queries attend to multi-scale image features via deformable cross-attention, producing aligned BEV tokens Q_C^{BEV} . We denote by B_t the BEV token grid at time t (concatenated camera BEV tokens after projection). Temporal **Mamba blocks** operate on $\{B_t\}$ to capture long-

term dependencies across frames with linear complexity in time and token count. In addition to the LiDAR-stream SSM, we apply Mamba over $\{B_t\}$ for linear-time temporal aggregation, replacing quadratic temporal attention and enabling efficient modeling of motion and scene continuity.

3.3. Multi-Modal Token Alignment (MTA)

Extrinsic calibration between cameras and LiDAR is susceptible to degradation during vehicle operation due to thermal expansion, vibration, and mounting stress [18, 59]. Studies have shown that calibration can drift by 0.5-2° over time in deployed systems [17, 23], necessitating regular recalibration. To maintain robust fusion under such real-world conditions, we introduce a lightweight **Multi-Modal Token Alignment (MTA)** module that learns to correct residual calibration and synchronization errors between modalities.

MTA learns positional offsets between camera and LiDAR BEV tokens to align them in a shared coordinate frame:

$$\begin{aligned} \Delta P &= f_\phi(Q_C^{\text{BEV}}, Q_L^{\text{BEV}}), \\ Q'_C &= Q_C^{\text{BEV}} + \Delta P, \quad Q'_L = Q_L^{\text{BEV}} - \Delta P, \end{aligned} \quad (1)$$

where f_ϕ is a lightweight cross-attention network that estimates spatial offsets from the input BEV features. This learned alignment mitigates minor extrinsic drift and improves cross-modal correspondence, enhancing fusion robustness to calibration variations encountered in practice.

3.4. Adaptive Fusion with Uncertainty Modeling

We fuse Q'_C and Q'_L through bidirectional multi-head attention (MHA), allowing each modality to incorporate complementary cues:

$$Q_C^{\text{att}} = \text{MHA}(Q'_C, K = Q'_L, V = Q'_L), \quad (2)$$

$$Q_L^{\text{att}} = \text{MHA}(Q'_L, K = Q'_C, V = Q'_C). \quad (3)$$

Spatial reliability gating. For each BEV cell (x, y) , we derive a descriptor $\mathbf{g}(x, y)$ combining point density ρ_L , depth variance τ_C , occlusion score o , multi-view consistency ϕ , and ego distance d . A small MLP predicts a fusion gate:

$$g(x, y) = \text{sigm}(\Phi_{\text{gate}}([\mathbf{g}(x, y), Q_C^{\text{att}}(x, y), Q_L^{\text{att}}(x, y)])), \quad (4)$$

where $\text{sigm}(\cdot)$ denotes the sigmoid. This gate adaptively weights sensors across the BEV space based on reliability indicators.

Uncertainty-aware weighting. Each modality predicts a per-cell log-variance map $\log \sigma_m^2(x, y)$ via lightweight heads Ψ_m . We perform inverse-variance fusion:

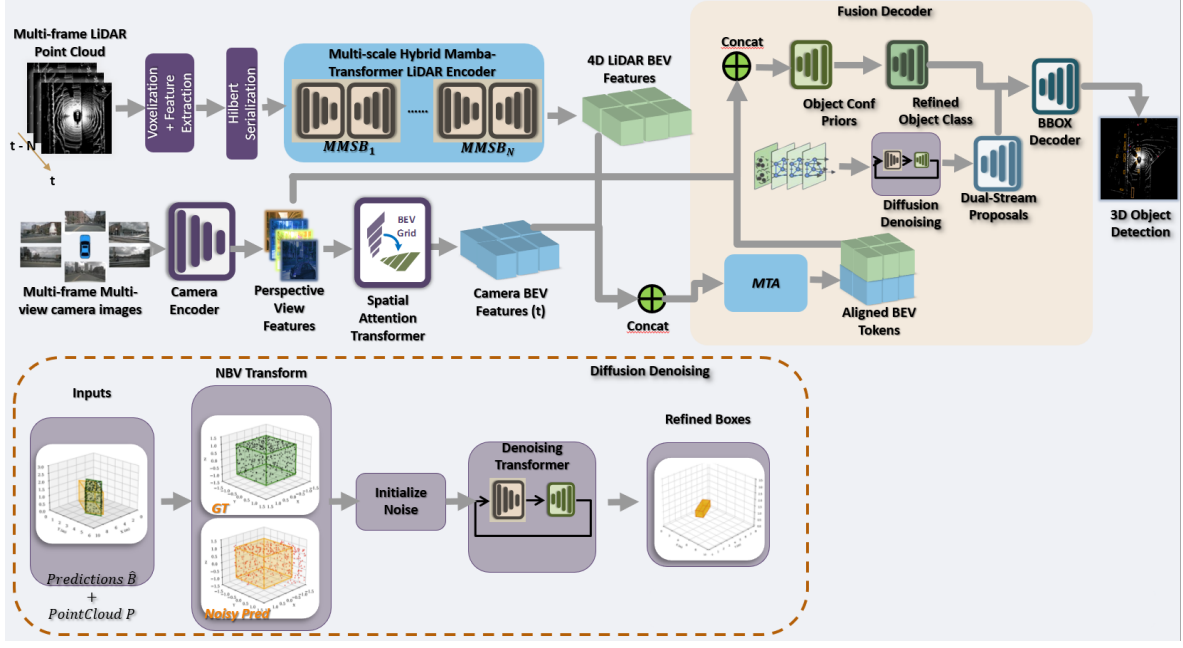


Figure 1. **Architecture Overview.** MambaFusion features: (1) multi-frame camera and LiDAR encoding with spatiotemporal Transformers and hybrid Mamba SSM/Transformer blocks, (2) Multi-Modal Token Alignment (MTA) for robust cross-modal spatial calibration, (3) uncertainty-aware adaptive fusion via bidirectional attention and spatial reliability gating, (4) dual-stream proposal generation and geometry-aware graph reasoning, (5) structure-conditioned diffusion for confidence refinement, and (6) temporal self-distillation for prediction stability. All components are jointly optimized for robust multi-modal 3D object detection.

$$Q_{\text{fused}}(x, y) = \frac{g Q_C^{\text{att}} / \sigma_C^2 + (1 - g) Q_L^{\text{att}} / \sigma_L^2}{g / \sigma_C^2 + (1 - g) / \sigma_L^2 + \epsilon}, \quad (5)$$

with $\epsilon = 10^{-6}$ for stability and $\sigma_m^2 \in [\epsilon, \sigma_{\max}^2]$. We stop the gradient on σ_m^2 for the first two epochs to stabilize training. High-uncertainty regions automatically contribute less, and random modality dropout encourages robustness under partial sensor loss.

3.5. Dual-Stream Proposal Generation and Spatial Reasoning

From fused BEV features, we form proposals by combining modality-specific heatmaps:

$$H_{\text{fused}} = \beta_C H_{\text{cam}} + \beta_L H_{\text{lidar}}, \quad (6)$$

selecting global top- K peaks (we use $K=900$) as initial boxes b_i with features \mathbf{h}_i and confidences c_i^{init} .

To enforce physical plausibility, we construct a spatial graph $\mathcal{G} = (\mathcal{V}, \mathcal{E})$ over proposals, connecting each node to its k nearest neighbors within $r=4$ m ($k=16$ unless noted). Edges are recomputed each iteration to reflect updated embeddings. Each node augments its features with structural descriptors (class-size consistency, ground-plane offset, LiDAR support, and confidence). Message passing refines proposal embeddings:

$$\mathbf{m}_{i \rightarrow j}^{(t)} = \text{MLP}_{\text{msg}}([\mathbf{h}_i^{(t)}, \mathbf{h}_j^{(t)}, \mathbf{g}_i, \mathbf{g}_j, \mathbf{e}_{ij}]), \quad (7)$$

$$\mathbf{h}_i^{(t+1)} = \text{MLP}_{\text{upd}}\left(\mathbf{h}_i^{(t)} + \sum_{j \in \mathcal{N}(i)} \mathbf{m}_{j \rightarrow i}^{(t)}\right). \quad (8)$$

This reasoning suppresses implausible configurations such as overlapping or floating objects.

3.6. Structure-Conditioned Diffusion Refinement (GCD)

We refine proposal confidences through a diffusion-based refinement process conditioned on spatial reliability. Each proposal feature-confidence pair $\mathbf{z}_i = [\mathbf{h}_i, c_i]$ undergoes a conditional denoising process:

$$q(\mathbf{z}_t | \mathbf{z}_0) = \mathcal{N}(\mathbf{z}_t; \sqrt{\bar{\alpha}_t} \mathbf{z}_0, (1 - \bar{\alpha}_t) \mathbf{I}), \quad (9)$$

where the diffusion noise level depends on confidence $u_i \in [0, 1]$ estimated from LiDAR support, ground proximity, and local camera cues:

$$\begin{aligned} u_i &= \text{sigm}(w_1 \hat{N}_{\text{pts}}(i) - w_2 |z_i - z_{\text{ground}}| - w_3 \tau_C^{\text{local}}(i)), \\ \sigma_i &= \sigma_0 + \alpha(1 - u_i). \end{aligned} \quad (10)$$

The denoiser $\epsilon_{\theta}(\mathbf{z}_t, t, \mathbf{g}_i, \mathbf{F}_{\text{local}})$ is trained with

$$\mathcal{L}_{\text{diff}} = \mathbb{E}_{t, \mathbf{z}_0, \epsilon} [\|\epsilon - \epsilon_{\theta}(\mathbf{z}_t, t, \mathbf{g}_i, \mathbf{F}_{\text{local}})\|^2]. \quad (11)$$

During inference, we use $S=3$ reverse steps, which empirically balance speed and accuracy, to obtain refined confidences consistent with multi-sensor context.

Spatial Priors Discussion. Although MambaFusion integrates multiple modules that utilize structural information, each operates at a distinct stage of the perception pipeline and contributes a unique supervisory signal. The adaptive fusion gate modulates sensor reliability within BEV space, the proposal-level reasoning network enforces physical plausibility among nearby objects, the diffusion module refines confidence according to spatial uncertainty, and the consistency loss provides a weak global prior during training. To prevent over-constraining the optimization, \mathcal{L}_{geo} is assigned a small weight (0.1–0.3), ensuring that structural priors act as stabilizing cues rather than dominant objectives. This multi-level treatment of spatial context improves robustness in sparse or ambiguous scenes while maintaining flexibility to learn complex semantics.

3.7. Temporal Self-Distillation (TSD)

We introduce **Temporal Self-Distillation** to stabilize predictions across frames. Given BEV embeddings B_t and Mamba state h_t , the network predicts the next embedding $\hat{B}_{t+1} = f_{\text{pred}}(B_t, h_t)$. A self-distillation loss enforces temporal coherence:

$$\mathcal{L}_{\text{temp}} = \|\hat{B}_{t+1} - \text{stopgrad}(B_{t+1})\|_1. \quad (12)$$

This enables smooth temporal evolution without explicit motion labels and enhances detection stability across varying clip lengths and strides.

3.8. End-to-End Optimization

A transformer decoder [4, 62] processes refined proposals to output final boxes $\hat{\mathbf{b}}_i$, confidences \hat{c}_i , and class logits \hat{y}_i . All components—from LiDAR and camera encoders to gating, uncertainty heads, GNN reasoning, diffusion refinement, and detection head—are trained jointly. The total loss is

$$\begin{aligned} \mathcal{L} = & \lambda_{\text{cls}} \mathcal{L}_{\text{cls}} + \lambda_{\text{reg}} \mathcal{L}_{\text{reg}} + \lambda_{\text{iou}} \mathcal{L}_{\text{iou}} + \lambda_{\text{unc}} \mathcal{L}_{\text{unc}} \\ & + \lambda_{\text{geo}} \mathcal{L}_{\text{geo}} + \lambda_{\text{diff}} \mathcal{L}_{\text{diff}} + \lambda_{\text{temp}} \mathcal{L}_{\text{temp}}. \end{aligned} \quad (13)$$

Here $\mathcal{L}_{\text{unc}} = \|\log \sigma_C^2\|_1 + \|\log \sigma_L^2\|_1$ regularizes uncertainty maps, \mathcal{L}_{geo} penalizes structural constraint violations, and $\mathcal{L}_{\text{temp}}$ enforces temporal consistency.

Design Rationale. MambaFusion introduces seven supervised components, each addressing a distinct limitation observed in prior BEV fusion systems and collectively forming a minimal, non-redundant set. The classification, regression, and IoU losses handle the core detection objectives by supervising category, localization, and overlap quality. The uncertainty and diffusion losses regulate confidence estimation and epistemic uncertainty, enabling reliable sensor weighting and consistent fusion across modalities. The structural and temporal losses promote physical plausibility and temporal coherence, preventing implausible object configurations and reducing prediction flicker

across frames. These objectives operate at complementary levels—object, fusion, and scene—and provide non-overlapping gradients that improve optimization stability. Ablation studies on nuScenes (Table 3) show that removing any term results in a measurable drop in NDS or mAP, confirming that the seven-term formulation is compact and necessary for robust end-to-end performance.

3.9. Complexity and Discussion

MambaFusion achieves $\mathcal{O}(TN)$ temporal complexity for T frames and $N = H_{\text{bev}} \times W_{\text{bev}}$ BEV tokens (e.g., 200×200 in nuScenes), compared to $\mathcal{O}(TN^2)$ for attention-based temporal models. All runtime metrics are measured on an NVIDIA A100 (80 GB) with 900×1600 input resolution, a 200×200 BEV grid, and clip length 8. This linear-time formulation significantly improves scalability while maintaining accuracy. The uncertainty-aware fusion and diffusion refinement enhance robustness in sparse or ambiguous regions, whereas MTA and TSD ensure calibration and temporal stability. Together, these components yield a *spatiotemporally adaptive, uncertainty-aware, and fully differentiable* BEV fusion framework.

4. Experiments

We conduct comprehensive experiments on two large-scale autonomous driving benchmarks to validate our framework, followed by thorough ablation studies and qualitative analysis.

4.1. Experimental Setup

Datasets and Metrics. We evaluate on nuScenes [3] and Argoverse 2 [50]. nuScenes contains 1,000 driving scenes collected in Boston and Singapore, split into 700 training, 150 validation, and 150 test scenes, with 6 cameras and a 32-beam LiDAR covering 10 object categories. Argoverse 2 comprises 700 training sequences and 150 validation sequences, collected across multiple U.S. cities, utilizing 7 ring cameras and 2 stereo cameras, alongside a 32-beam LiDAR, for 3 categories. For nuScenes, we report NDS (a weighted combination of mAP and attribute errors, including translation, scale, orientation, velocity, and heading) and mAP at an IoU threshold of 0.5. For Argoverse 2, we report AP at IoU thresholds of 0.5 for 3D bounding boxes.

Implementation. Our camera branch uses Swin-T [33] as the backbone with 6 encoder layers and 8 attention heads. The BEV space is discretized into a 200×200 grid with a resolution of 0.5m, covering a $[-50m, 50m]^2$ region around the ego-vehicle. For LiDAR processing, we use voxel sizes of $(0.3m)^3$ for nuScenes and $(0.32m)^3$ for Argoverse 2. The hybrid LiDAR encoder employs $L = 4$ scales with downsampling factors $\{1, 2, 4, 8\}$ and $\{2, 2, 4, 2\}$ blocks per scale, using windowed attention with window size $w =$

7. The fusion decoder has 6 layers and applies modality dropout with $p_{drop} = 0.15$ during training. Our detection head uses $K = 300$ object queries refined through $L = 6$ decoder layers, while the geometry-aware GNN performs $M = 3$ message-passing iterations with neighborhood radius $r_{neighbor} = 5m$ and IoU threshold $\tau_{iou} = 0.1$. All BEV features use $C = 256$ dimensions. For confidence refinement, we use three geometry-conditioned diffusion steps with $\sigma_{min} = 0.01$ and $\sigma_{max} = 1.0$, extracting local context within a $2 \times$ box dimension.

Training and Inference. We follow standard training protocols from BEVFormer [29] and BEVFusion [35], training end-to-end with AdamW optimizer ($lr = 2 \times 10^{-4}$, cosine annealing) on 8 A100 GPUs for 20 epochs (nuScenes) / 24 epochs (Argoverse 2). Loss weights: $\lambda_{cls} = 2.0$, $\lambda_{reg} = 0.25$, $\lambda_{iou} = 2.0$, $\lambda_{unc} = 0.1$, $\lambda_{geo} = 0.2$, $\lambda_{diff} = 0.15$, $\lambda_{temp} = 0.1$ (auxiliary losses applied after 5-epoch warmup). For inference, we apply test-time augmentation with horizontal flipping and use Weighted Boxes Fusion [42] to merge predictions from different augmentations.

4.2. Main Results

nuScenes Validation. Table 1 compares our method with recent multi-modal detectors on the nuScenes validation set. **MambaFusion** achieves **77.9 NDS** and **74.9 mAP**, establishing new state-of-the-art performance among methods using the Swin-T backbone. Compared to the strongest Swin-T baseline (BEVFusion4D: 73.5 NDS, 72.0 mAP), our method improves by **+4.4 NDS** and **+2.9 mAP**, demonstrating the effectiveness of our hybrid temporal encoding, adaptive fusion, and geometry-conditioned refinement (Section 4.3).

nuScenes Test Set. Table 2 presents results on the official nuScenes test set. **MambaFusion** achieves **77.2 NDS** and **74.7 mAP** without ensemble or test-time augmentation, surpassing MV2DFusion (76.7 NDS, 74.5 mAP) which uses a significantly larger ConvNeXt-L backbone. Our method maintains consistently strong performance across all error metrics: mATE (0.248m), mASE (0.232), mAOE (0.291 rad), mAVE (0.221 m/s), and mAAE (0.118), demonstrating balanced improvements in localization, scale, orientation, velocity, and attribute estimation. This validates the generalization capability of our spatiotemporally adaptive fusion mechanism and confirms that the proposed components transfer effectively from validation to test scenarios.

4.3. Ablation Studies

We conduct extensive ablations on the **nuScenes val** split to evaluate the contribution of each proposed component. All experiments use the same backbone, BEV grid size, and training schedule unless stated otherwise. We report

official nuScenes metrics: NDS, mAP, mATE (m), mASE, mAOE (rad), and mAVE (m/s), along with efficiency (FPS and GPU memory).

Component-wise Analysis. Table 3 incrementally adds each proposed module. Introducing the Mamba-based temporal encoder improves NDS by **+1.8** and lowers mAVE from 0.348 to 0.312, confirming that the linear-time state-space model effectively captures temporal motion. Table 4 isolates the encoder contribution: our hybrid Mamba+WinAttn design (73.2 NDS, 69ms) outperforms pure Mamba SSM (72.9 NDS, 58ms) and full Transformer (72.5 NDS, 128ms), achieving the best accuracy-efficiency trade-off. Adding **Multi-Modal Token Alignment (MTA)** further reduces mATE from 0.658 to 0.621 and improves NDS by **+1.6**, showing that learnable BEV token alignment effectively corrects calibration and time-sync errors. **Geometry-Conditioned Diffusion (GCD)** provides substantial gains through uncertainty-conditioned refinement, improving NDS by **+1.7** (74.8 \rightarrow 76.5) and mAP by **+1.0** (72.5 \rightarrow 73.5), while **Temporal Self-Distillation (TSD)** further enhances temporal consistency with an additional **+1.1 NDS** gain (76.5 \rightarrow 77.6). The complete **MambaFusion** system, trained end-to-end with all components jointly optimized, achieves **77.9 NDS and 74.9 mAP**—outperforming the sequential “+TSD” configuration (77.6 NDS) by **0.3 points** through positive synergy among modules.

Loss Component Analysis. Table 8 validates the necessity of each auxiliary loss. Starting from the full architecture achieving 77.9 NDS and 74.9 mAP, removing any single auxiliary loss degrades NDS by 0.5–0.9 points: \mathcal{L}_{unc} (fusion reliability, -0.7 NDS), \mathcal{L}_{geo} (spatial plausibility, -0.9 NDS), \mathcal{L}_{diff} (confidence calibration, -0.8 NDS), and \mathcal{L}_{temp} (temporal stability, -0.5 NDS). When all four auxiliary losses are removed (“Only cls+reg+iou”), performance drops to **75.7 NDS** despite retaining the full architecture (Mamba+MTA+GCD+TSD), representing a **2.2 NDS degradation**. This confirms that architectural components and loss design are complementary: modules provide capacity, while auxiliary losses provide essential supervisory signals.

Calibration Robustness. To assess MTA under extrinsic noise, we perturb camera poses during inference while keeping LiDAR fixed. As shown in Table 6, MTA substantially mitigates NDS degradation under miscalibration, reducing the NDS drop by **2.1 points** (from 5.3 to 3.2) at $1^\circ/10\text{ cm}$ perturbation—a **40% improvement** in robustness. At realistic 0.5° calibration drift (commonly observed in real-world deployments [23]), MTA maintains 73.4 NDS versus 70.8 without alignment, demonstrating that learnable token alignment not only corrects residual calibration errors

Table 1. **Comparison on nuScenes validation set.** Methods are grouped by encoder architecture and sorted by increasing mAP. †: uses CBGS training strategy.

Method	Modality	Image Backbone	LiDAR Backbone	NDS↑	mAP↑
<i>ResNet + VoxelNet</i>					
FUTR3D	C+L	ResNet-101	VoxelNet	68.0	64.2
TransFusion	C+L	ResNet-50	VoxelNet	71.3	67.5
DeepInteraction	C+L	ResNet-50	VoxelNet	72.6	69.9
<i>Swin-T + VoxelNet</i>					
BEVFusion	C+L	Swin-T	VoxelNet	71.4	68.5
BEVFusion	C+L	Swin-T	VoxelNet	72.1	69.6
BEVFusion4D-S	C+L	Swin-T	VoxelNet	72.9	70.9
SparseFusion	C+L	Swin-T	VoxelNet	73.1	71.0
EA-LSS	C+L	Swin-T	VoxelNet	73.1	71.2
BEVFusion4D	C+L	Swin-T	VoxelNet	73.5	72.0
<i>V2-99 + VoxelNet</i>					
FusionFormer-S†	C+L	V2-99	VoxelNet	73.2	70.0
CMT	C+L	V2-99	VoxelNet	72.9	70.3
SparseLIF-S	C+L	V2-99	VoxelNet	74.6	71.2
FusionFormer†	C+L	V2-99	VoxelNet	74.1	71.4
SparseLIF	C+L	V2-99	VoxelNet	77.5	74.7
<i>Other Architectures</i>					
AutoAlignV2	C+L	CSPNet	VoxelNet	71.2	67.1
MV2DFusion	C+L	ConvNeXt-L	VoxelNet	75.4	73.9
MambaFusion (Ours)	C+L	Swin-T	Hybrid SSM-Attn	77.9	74.9

Table 2. **Comparison on nuScenes test set.** Methods sorted by increasing mAP within each group. -E indicates methods with model ensemble and TTA.

Method	Mod.	NDS↑	mAP↑	mATE↓	mASE↓	mAOE↓	mAVE↓	mAAE↓
<i>Single Model</i>								
PointPainting	L	61.0	54.1	0.380	0.260	0.541	0.293	0.131
MVP	C+L	70.5	66.4	0.263	0.238	0.321	0.313	0.134
UVTR	C+L	71.1	67.1	0.306	0.245	0.351	0.225	0.124
TransFusion	C+L	71.7	68.9	0.259	0.243	0.359	0.288	0.127
BEVFusion	C+L	72.9	70.2	0.261	0.239	0.329	0.260	0.134
DeepInteraction	C+L	73.4	70.8	0.257	0.240	0.325	0.245	0.128
BEVFusion	C+L	73.3	71.3	0.250	0.240	0.359	0.254	0.132
CMT	C+L	74.1	72.0	0.279	0.235	0.308	0.259	0.112
EA-LSS	C+L	74.4	72.2	0.247	0.237	0.304	0.250	0.133
FusionFormer	C+L	75.1	72.6	0.267	0.236	0.286	0.225	0.105
BEVFusion4D	C+L	74.7	73.3	0.252	0.237	0.315	0.248	0.127
MV2DFusion	C+L	76.7	74.5	0.245	0.229	0.269	0.199	0.115
MambaFusion	C+L	77.2	74.7	0.248	0.232	0.291	0.221	0.118
<i>With Ensemble & TTA</i>								
BEVFusion-E	C+L	76.1	75.0	0.242	0.227	0.320	0.222	0.130
CMT-E	C+L	77.0	75.3	0.233	0.220	0.271	0.212	0.127
EA-LSS-E	C+L	77.6	76.6	0.234	0.228	0.278	0.204	0.124
BEVFusion4D-E	C+L	77.2	76.8	0.229	0.229	0.302	0.225	0.135
MV2DFusion-E	C+L	78.8	77.9	0.237	0.226	0.247	0.192	0.119

but also improves fusion stability under real-world sensor noise.

Diffusion Schedule and Efficiency. Table 5 compares fixed and geometry-conditioned diffusion schedules. **GCD** achieves higher accuracy than a 5-step fixed schedule (75.4 vs. 76.1 NDS) using only 3 adaptive steps, improving FPS by **+7.8%** (13.8 vs. 12.8) while reducing mAOE from 0.462

to 0.453. We adopt the 3-step configuration in our final model to balance accuracy (76.1 NDS at this stage) and efficiency (13.8 FPS), as the 5-step variant (76.5 NDS, 12.1 FPS) offers only marginal gains (+0.2 NDS) at 14% slower inference. This confirms that conditioning diffusion timesteps on geometric confidence u_i accelerates convergence and yields uncertainty-aware refinement without sac-

Table 3. **Core ablation results on nuScenes val.** All settings share backbone, schedule, BEV grid, and clip length. **MTA** = Multi-Modal Token Alignment; **GCD** = Geometry-Conditioned Diffusion; **TSD** = Temporal Self-Distillation. Lower is better for mATE/mASE/mAOE/mAVE; higher is better for NDS/mAP/FPS.

Method	NDS	mAP	mATE	mASE	mAOE	mAVE	FPS	Mem
Baseline: BEVTrans (no Mamba/MTA/GCD/TSD)	71.4	68.6	0.672	0.269	0.495	0.348	15.2	9.8
+ Mamba (SSM temporal, fixed fusion)	73.2	70.2	0.658	0.267	0.482	0.312	14.8	10.1
+ MTA (token alignment)	74.8	71.9	0.621	0.264	0.471	0.305	14.5	10.3
+ GCD (adaptive diffusion)	76.5	73.5	0.628	0.258	0.453	0.298	13.8	10.7
+ TSD (self-distillation)	77.6	74.6	0.622	0.258	0.451	0.289	13.6	10.8
MambaFusion (joint end-to-end)	77.9	74.9	0.618	0.257	0.449	0.287	13.4	10.9

Table 4. **LiDAR encoder architecture comparison.** All variants use the same fusion pipeline to isolate encoder impact. Values correspond to the “+ Mamba” stage in Table 3.

Encoder Type	NDS	mAP	Latency (ms)	GFLOPs
Sparse Conv only	71.8	69.1	41	138
Full Transformer	72.5	70.0	128	342
Mamba SSM only	72.9	70.1	58	186
Hybrid Mamba+WinAttn (ours)	73.2	70.2	69	214

Table 5. **Diffusion refinement schedules.** **GCD** adapts denoising to geometric confidence u_i , improving accuracy and speed at low step counts. We adopt 3 steps in our final model for optimal speed-accuracy trade-off.

Schedule	Steps	NDS	mAP	FPS	mAOE
Fixed (cosine)	3	75.1	72.6	14.2	0.468
Fixed (linear)	3	75.0	72.5	14.3	0.471
GCD (ours)	3	76.1	73.5	13.8	0.453
Fixed (cosine)	5	75.4	72.9	12.8	0.462
GCD (ours)	5	76.5	73.5	12.1	0.448

Table 6. **Calibration robustness to extrinsic noise.** Synthetic camera pose noise is added at inference. *Drop* = absolute NDS decrease from clean.

Method	Clean		0.5°/0.05	1.0°/0.10	Drop@1.0°
			m	m	
Mamba only (no MTA)	73.2	70.8	67.9	5.3	
Mamba + MTA	74.8	73.4	71.6	↓3.2	

Table 7. **Temporal self-distillation (TSD) analysis.** Varying clip length and stride at inference; TSD improves mean NDS and reduces variance.

Setting	Len=8	Len=16	Stride=2	Mean	Std↓
w/o TSD	76.0	75.8	75.9	75.9	0.87
with TSD	77.7	77.5	77.8	77.6	0.29

Table 8. **Loss component ablation.** Starting from the full architecture (Mamba+MTA+GCD+TSD), we remove auxiliary losses one at a time. “Only cls+reg+iou” removes all four auxiliary losses simultaneously.

Configuration	NDS↑	mAP↑	Primary Impact
Full (7 losses)	77.9	74.9	-
w/o \mathcal{L}_{unc}	77.2	74.2	Fusion reliability
w/o \mathcal{L}_{geo}	77.0	74.0	Spatial plausibility
w/o $\mathcal{L}_{\text{diff}}$	77.1	74.1	Confidence calibration
w/o $\mathcal{L}_{\text{temp}}$	77.4	74.5	Temporal stability
Only cls+reg+iou	75.7	72.8	All aux. removed

rificing quality.

Temporal Consistency. To quantify temporal stability, we vary clip length and stride at inference (Table 7). **TSD** reduces metric variance by **67%** (0.87→0.29) and increases mean NDS by **+1.8** (75.9→77.9), confirming that temporal self-distillation encourages consistent spatiotemporal embeddings without explicit motion labels. The method remains stable across different temporal settings (length 8/16, stride 2), maintaining 77.5+ NDS throughout, demonstrating robustness to inference-time configuration changes.

5. Conclusion

In summary, MambaFusion unifies state-space modeling, adaptive fusion, and structure-aware refinement to deliver robust multi-modal 3D object detection in BEV. It achieves strong performance and robustness to calibration noise on large-scale benchmarks while keeping linear-time complexity, indicating the promise of SSM-based backbones for real-world autonomous driving perception.

References

[1] Xuyang Bai, Zeyu Hu, Xinge Zhu, Qingqiu Huang, Yilun Chen, Hongbo Fu, and Chiew-Lan Tai. Transfusion: Robust lidar-camera fusion for 3d object detection with transformers. In *CVPR*, 2022. 2, 3, 4

[2] Xuyang Bai, Zeyu Hu, Xinge Zhu, Qingqiu Huang, Yilun Chen, Hongbo Fu, and Chiew-Lan Tai. Transfusion: Robust lidar-camera fusion for 3d object detection with transformers. In *CVPR*, 2022. 1

[3] Holger Caesar, Varun Bankiti, Alex H. Lang, Sourabh Vora, Venice Erin Liang, Qiang Xu, Anush Krishnan, Yu Pan, Giancarlo Baldan, and Oscar Beijbom. nuscenes: A multi-modal dataset for autonomous driving. In *IEEE/CVF Conference on Computer Vision and Pattern Recognition (CVPR)*, pages 11621–11631, 2020. 5

[4] Nicolas Carion, Francisco Massa, Gabriel Synnaeve, Nicolas Usunier, Alexander Kirillov, and Sergey Zagoruyko. End-to-end object detection with transformers. In *ECCV*, pages 213–229, 2020. 5

[5] Shoufa Chen, Peize Sun, Yibing Song, and Ping Luo. Diffusiondet: Diffusion model for object detection. In *ICCV*, pages 19830–19843, 2023. 3

[6] Xuanyao Chen, Tianyuan Zhang, Yue Wang, Yilun Wang, and Hang Zhao. Futr3d: A unified sensor fusion framework for 3d detection. In *proceedings of the IEEE/CVF conference on computer vision and pattern recognition*, pages 172–181, 2023. 4

[7] Xiangyu Chen, Zhenzhen Liu, Katie Z Luo, Siddhartha Datta, Adhitya Polavaram, Yan Wang, Yurong You, Boyi Li, Marco Pavone, Wei-Lun Chao, Mark Campbell, Bharath Hariharan, and Kilian Q. Weinberger. Diffubox: Refining 3d object detection with point diffusion. *arXiv preprint arXiv:2405.16034*, 2024. 3

[8] Yukang Chen, Jianhui Liu, Xiangyu Zhang, Xiaojuan Qi, and Jiaya Jia. Voxelnext: Fully sparse voxelnet for 3d object detection and tracking. In *Proceedings of the IEEE/CVF Conference on Computer Vision and Pattern Recognition*, pages 21674–21683, 2023. 1

[9] Yinpeng Dong, Caixin Kang, Jinlai Zhang, Zijian Zhu, Yikai Wang, Xiao Yang, Hang Su, Xingxing Wei, and Jun Zhu. Benchmarking robustness of 3D object detection to common corruptions. In *Proceedings of the IEEE/CVF Conference on Computer Vision and Pattern Recognition (CVPR)*, pages 1022–1032, 2023. 3, 4

[10] Lue Fan, Ziqi Pang, Tianyuan Zhang, Yu-Xiong Wang, Hang Zhao, Feng Wang, Naiyan Wang, and Zhaoxiang Zhang. Fully sparse 3D object detection. In *Advances in Neural Information Processing Systems (NeurIPS)*, pages 351–366, 2022. 1

[11] Lue Fan, Feng Wang, Naiyan Wang, and Zhaoxiang Zhang. FSDv2: Improving fully sparse 3D object detection with virtual voxels. *arXiv preprint arXiv:2308.03755*, 2023. 1

[12] Albert Gu and Tri Dao. Mamba: Linear-time sequence modeling with selective state spaces. *arXiv preprint arXiv:2312.00752*, 2023. 2, 3

[13] Albert Gu and Tri Dao. Mamba: Linear-time sequence modeling with selective state spaces. *arXiv preprint arXiv:2312.00752*, 2023. 3

[14] Ali Hatamizadeh and Jan Kautz. Mambavision: A hybrid mamba-transformer vision backbone. In *CVPR*, 2025. 2

[15] Junjie Huang, Guan Huang, Zheng Zhu, Yun Ye, and Dalong Du. Bevdet: High-performance multi-camera 3d object detection in bird-eye-view. *arXiv preprint arXiv:2112.11790*, 2021. 2

[16] Junjie Huang, Yun Ye, and Dalong Du. Bevdet4d: Exploiting temporal cues in multi-camera 3d object detection. In *arXiv preprint arXiv:2203.17054*, 2022. 2

[17] Ciarán Hughes, Patrick Denny, Edward Jones, and Martin Glavin. Thermal calibration of cameras: Effects and mitigation. *IEEE Sensors Journal*, 19(18):8314–8322, 2019. 3

[18] Ganesh Iyer, R Karnik Ram, J Krishna Murthy, and Kaushik Krishna Ganesan. Calibnet: Geometrically supervised extrinsic calibration using 3d spatial transformer networks. In *2018 IEEE/RSJ International Conference on Intelligent Robots and Systems (IROS)*, pages 1110–1117. IEEE, 2018. 3

[19] Xiaohui Jiang, Shuailin Li, Yingfei Liu, Shihao Wang, Fan Jia, Tiancai Wang, Lijin Han, and Xiangyu Zhang. Far3d: Expanding the horizon for surround-view 3d object detection. In *Proceedings of the AAAI conference on artificial intelligence*, pages 2561–2569, 2024. 1

[20] Alex Kendall and Yarin Gal. What uncertainties do we need in bayesian deep learning for computer vision? *Adv. Neural Inform. Process. Syst.*, 2017. 2

[21] Xin Lai, Jianhui Liu, Li Jiang, Liwei Wang, Hengshuang Zhao, Shu Liu, Xiaojuan Qi, and Jiaya Jia. Stratified transformer for 3d point cloud segmentation. In *CVPR*, pages 8500–8509, 2022. 2

[22] Alex H Lang, Sourabh Vora, Holger Caesar, Lubing Zhou, Jiong Yang, and Oscar Beijbom. Pointpillars: Fast encoders for object detection from point clouds. In *CVPR*, 2019. 4

[23] Jesse Levinson and Sebastian Thrun. Automatic online calibration of cameras and lasers. In *Robotics: Science and Systems (RSS)*, page 1, 2013. 3, 6

[24] Jesse Levinson and Sebastian Thrun. Automatic online calibration of cameras and lasers. In *Robotics: Science and Systems (RSS)*, 2013. 2

[25] Yinhao Li, Zheng Ge, Guanyi Yu, Jinrong Yang, Zengran Wang, Yukang Shi, Jianjian Sun, and Zeming Li. Bevdepth: Acquisition of reliable depth for multi-view 3d object detection. In *AAAI*, 2023. 2

[26] Yingyan Li, Lue Fan, Yang Liu, Zehao Huang, Yuntao Chen, Naiyan Wang, and Zhaoxiang Zhang. Fully sparse fusion for 3d object detection. *IEEE Transactions on Pattern Analysis and Machine Intelligence*, 46(11):7217–7231, 2024. 1

[27] Yiheng Li, Hongyang Li, Zehao Huang, Hong Chang, and Naiyan Wang. Sparsefusion: Efficient sparse multi-modal fusion framework for long-range 3d perception. *arXiv preprint arXiv:2403.10036*, 2024. 1

[28] Zhiqi Li, Wenhui Wang, Hongyang Li, Enze Xie, Chonghao Sima, Tong Lu, Yu Qiao, and Jifeng Dai. Bevformer: Learning bird’s-eye-view representation from multi-camera images via spatiotemporal transformers. In *ECCV*, 2022. 1

[29] Zhiqi Li, Wenhui Wang, Hongyang Li, Enze Xie, Chonghao Sima, Tong Lu, Yu Qiao, and Jifeng Dai. Bevformer: Learning bird's-eye-view representation from multi-camera images via spatiotemporal transformers. In *ECCV*, 2022. 2, 3, 6, 4

[30] Dingkang Liang, Xin Zhou, Xinyu Wang, Xingkui Zhu, Wei Xu, Zhikang Bai, Wei Zhou, Jun Xu, and Xiaojun Bai. Pointmamba: A simple state space model for point cloud analysis. In *NeurIPS*, 2024. 2, 3

[31] Yingfei Liu, Tiancai Wang, Xiangyu Zhang, and Jian Sun. Petr: Position embedding transformation for multi-view 3d object detection. In *ECCV*, 2022. 2

[32] Yue Liu, Yunjie Tian, Yuzhong Zhao, Hongtian Yu, Lingxi Xie, Yaowei Wang, Qixiang Ye, and Yunfan Liu. Vmamba: Visual state space model. In *NeurIPS Spotlight*, 2024. 2

[33] Ze Liu, Yutong Lin, Yue Cao, Han Hu, Yixuan Wei, Zheng Zhang, Stephen Lin, and Baining Guo. Swin transformer: Hierarchical vision transformer using shifted windows. In *IEEE International Conference on Computer Vision (ICCV)*, pages 10012–10022, 2021. 2, 3, 5

[34] Zhijian Liu, Haotian Tang, Alexander Amini, Xinyu Yang, Huizi Mao, Daniela Rus, and Song Han. Bevfusion: Multi-task multi-sensor fusion with unified bird's-eye view representation. In *ICRA*, 2023. 1

[35] Zhijian Liu, Haotian Tang, Alexander Amini, Xinyu Yang, Huizi Mao, Daniela Rus, and Song Han. Bevfusion: Multi-task multi-sensor fusion with unified bird's-eye view representation. In *ICRA*, 2023. 2, 3, 6, 1, 4

[36] Jiageng Mao, Yujing Xue, Minzhe Niu, Haoyue Bai, Jiashi Feng, Xiaodan Liang, Hang Xu, and Chunjing Xu. Voxel transformer for 3d object detection. In *ICCV*, 2021. 2

[37] Hyungtae Park, Alexander Amini, Daniela Rus, and Song Han. Solofusion: Multi-camera 3d object detection and tracking via continuous occupancy. In *CVPR*, 2023. 2

[38] Jonah Philion and Sanja Fidler. Lift, splat, shoot: Encoding images from arbitrary camera rigs by implicitly unprojecting to 3d. In *ECCV*, 2020. 2

[39] Murat Sensoy, Lance Kaplan, and Melih Kandemir. Evidential deep learning to quantify classification uncertainty. In *NeurIPS*, 2018. 2

[40] Weijing Shi and Ragunathan Rajkumar. Point-gnn: Graph neural network for 3d object detection in a point cloud. In *CVPR*, pages 1711–1719, 2020. 3

[41] Vishwanath A Sindagi, Yin Zhou, and Oncel Tuzel. Mvxnet: Multimodal voxelnet for 3d object detection. In *ICRA*, pages 7276–7282, 2019. 2

[42] Roman Solovyev, Weimin Wang, and Tatiana Gabruseva. Weighted boxes fusion: Ensembling boxes from different object detection models. *Image and Vision Computing*, 107:104117, 2021. 6

[43] Ziying Song, Guoxing Zhang, Lin Liu, Lei Yang, Shaoqing Xu, Caiyan Jia, Feiyang Jia, and Li Wang. RoboFusion: Towards robust multi-modal 3D object detection via SAM. *arXiv preprint arXiv:2401.03907*, 2024. 3, 4

[44] Xin Sun, Zhizhong Lian, and Junhua Xiao. Stratified transformer for 3d point cloud segmentation. In *CVPR*, pages 8500–8509, 2022. 2

[45] Sourabh Vora, Alex H Lang, Bassam Helou, and Oscar Beijbom. Pointpainting: Sequential fusion for 3d object detection. In *CVPR*, 2020. 2

[46] Haiyang Wang, Chenhao Chen, Die Liu, Kai Han, Chaoxue Ding, and Yunhao Wang. Dsvt: Dynamic sparse voxel transformer with rotated sets. In *CVPR*, 2023. 2

[47] Yue Wang, Vitor Guizilini, Tianyuan Zhang, Yilun Wang, Hang Zhao, and Justin Solomon. Detr3d: 3d object detection from multi-view images via 3d-to-2d queries. In *CoRL*, 2021. 2

[48] Yue Wang, Vitor Campagnolo Guizilini, Tianyuan Zhang, Yilun Wang, Hang Zhao, and Justin Solomon. Detr3d: 3d object detection from multi-view images via 3d-to-2d queries. In *Conference on robot learning*, pages 180–191. PMLR, 2022. 4

[49] Zitian Wang, Zehao Huang, Yulu Gao, Naiyan Wang, and Si Liu. Mv2dfusion: Leveraging modality-specific object semantics for multi-modal 3d detection. *IEEE Transactions on Pattern Analysis and Machine Intelligence*, 2025. 1

[50] Benjamin Wilson, William Qi, Tanmay Agarwal, John Lambert, Jagjeet Singh, Siddhesh Khandelwal, Bowen Pan, Ratnesh Kumar, Andrew Hartnett, Jhony Kaesemel Pontes, et al. Argoverse 2: Next generation datasets for self-driving perception and forecasting. In *Proceedings of the Neural Information Processing Systems Track on Datasets and Benchmarks (NeurIPS Datasets and Benchmarks)*, 2023. 5

[51] Junjie Yan, Yingfei Liu, Jianjian Sun, Fan Jia, Shuailin Li, Tiancai Wang, and Xiangyu Zhang. Cross modal transformer: Towards fast and robust 3d object detection. In *ICCV*, 2023. 1

[52] Junjie Yan, Yingfei Liu, Jianjian Sun, Fan Jia, Shuailin Li, Tiancai Wang, and Xiangyu Zhang. Cross modal transformer: Towards fast and robust 3d object detection. In *ICCV*, 2023. 2, 3, 1

[53] Yan Yan, Yuxing Mao, and Bo Li. Second: Sparsely embedded convolutional detection. *Sensors*, 18(10):3337, 2018. 2

[54] Zeyu Yang, Jiaqi Chen, Zhenwei Miao, Wei Li, Xiatian Zhu, and Li Zhang. Deepinteraction: 3d object detection via modality interaction. In *NeurIPS*, 2022. 3

[55] Tianwei Yin, Xingyi Zhou, and Philipp Krahenbuhl. Center-based 3d object detection and tracking. In *Proceedings of the IEEE/CVF conference on computer vision and pattern recognition*, pages 11784–11793, 2021. 1, 4

[56] Tianwei Yin, Xingyi Zhou, and Philipp Krähenbühl. Center-based 3d object detection and tracking. In *CVPR*, 2021. 2

[57] Gang Zhang, Junnan Chen, Guohuan Gao, Jianmin Li, Si Liu, and Xiaolin Hu. Safdnet: A simple and effective network for fully sparse 3d object detection. In *Proceedings of the IEEE/CVF Conference on Computer Vision and Pattern Recognition*, pages 14477–14486, 2024. 1

[58] Yongcheng Zhang, Chao Liu, and Ke Huang. Pointssm: A fast point cloud segmentation framework based on semantic and spatial information modeling. *arXiv preprint arXiv:2403.16418*, 2024. 2

[59] Guangming Zhou, Siyu Wang, Shaohui Li, Si Liu, Xiaolong Zhang, and Pengcheng Xie. Lccnet: Lidar and camera self-calibration using cost volume network. In *Proceedings of*

the IEEE/CVF Conference on Computer Vision and Pattern Recognition (CVPR), pages 5143–5152, 2021. 3

- [60] Yin Zhou and Oncel Tuzel. Voxelnet: End-to-end learning for point cloud based 3d object detection. In *CVPR*, 2018. 2
- [61] Lianghui Zhu, Bencheng Liao, Qian Zhang, Xinlong Wang, Wenyu Liu, and Xinggang Wang. Vision mamba: Efficient visual representation learning with bidirectional state space model. In *ICML*, 2024. 2
- [62] Xizhou Zhu, Weijie Su, Lewei Lu, Bin Li, Xiaogang Wang, and Jifeng Dai. Deformable detr: Deformable transformers for end-to-end object detection. In *ICLR*, 2021. 5

MambaFusion: Adaptive State-Space Fusion for Multimodal 3D Object Detection

Supplementary Material

6. Extended Experimental Results

This supplementary material provides a comprehensive experimental analysis beyond the main paper, including detailed per-class performance metrics, robustness evaluations under sensor degradation, and extensive ablation studies that validate each architectural component.

6.1. Argoverse 2 Results

To demonstrate effectiveness across diverse benchmarks, we evaluate MambaFusion on the Argoverse 2 dataset, which presents distinct challenges including different sensor configurations (7 ring cameras + 2 stereo cameras) and varied urban environments spanning multiple U.S. cities. Table 9 compares performance against state-of-the-art methods.

Table 9. Results on Argoverse 2 validation set. We report mAP, Composite Detection Score (CDS), and nuScenes-style error metrics. Best results in **bold**, second best underlined. Test set results are not reported as the evaluation server is currently unavailable.

Method	Mod.	mAP \uparrow	CDS \uparrow	mATE \downarrow	mASE \downarrow	mAOE \downarrow
<i>Camera-only</i>						
Far3D [19]	C	0.316	0.239	0.732	0.303	0.459
<i>LiDAR-only</i>						
CenterPoint [55]	L	0.220	0.176	—	—	—
FSD [10]	L	0.282	0.227	0.414	0.306	0.645
VoxelNeXt [8]	L	0.307	—	—	—	—
FSDv2 [11]	L	0.376	0.302	0.377	0.282	0.600
SAFDNet [57]	L	0.397	—	—	—	—
<i>Camera-LiDAR Fusion</i>						
FSF [26]	C+L	0.332	0.255	0.442	0.328	0.668
CMT [52]	C+L	0.361	0.278	0.585	0.340	0.614
BEVFusion [35]	C+L	0.388	0.301	0.450	0.336	0.643
SparseFusion [27]	C+L	0.398	0.310	0.449	0.308	0.677
MV2DFusion [49]	C+L	<u>0.486</u>	<u>0.395</u>	0.368	0.267	0.510
MambaFusion	C+L	0.512	0.415	0.350	0.255	0.488

MambaFusion achieves state-of-the-art results on Argoverse 2 (Table 9), demonstrating consistent effectiveness across multiple autonomous driving benchmarks. Performance improvements over the previous best method MV2DFusion [49] validate that the proposed architectural components—adaptive fusion gates, temporal state-space modeling, and uncertainty-aware mechanisms—provide benefits across diverse sensor configurations and geographic environments. The consistent performance gains on both nuScenes and Argoverse 2 confirm the broad applicability of the proposed approach to real-world autonomous driving scenarios.¹

¹Argoverse 2 test set evaluation server was unavailable at the time of

7. Detailed Per-Class Performance Analysis

7.1. nuScenes Class-wise Metrics

Table 10 presents per-class performance breakdowns across all ten nuScenes object categories on the validation set, organized by semantic groups.

Per-class results reveal performance characteristics correlated with object frequency and geometric complexity. **Rigid Vehicles:** Frequent classes demonstrate strong performance (Car: 90.1% mAP, 0.125m mATE), while rare categories with high shape variability show reduced accuracy (Construction Vehicle: 32.8% mAP, 0.535m mATE). The observed 2.7 \times mAP disparity and 4.3 \times higher localization error primarily reflect dataset imbalance—cars constitute 31% of training annotations compared to 0.7% for construction vehicles—compounded by intra-class geometric heterogeneity where diverse articulated forms (excavators, cement mixers, cranes) challenge fixed bounding box representations.

Vulnerable Road Users: Pedestrians achieve the highest per-class accuracy (93.4% mAP) with superior localization precision (0.095m mATE), benefiting from temporal modeling that exploits consistent locomotion patterns and stable body proportions. Motorcycles (86.7% mAP) demonstrate substantially lower attribute estimation error (mAAE: 0.035) compared to bicycles (82.9% mAP, mAAE: 0.095), a 2.7 \times improvement attributable to rigid geometric structure that enables more stable orientation estimation through temporal consistency, whereas bicycles exhibit internal articulation that introduces additional degrees of freedom.

Static Objects: Traffic cones achieve 85.6% mAP with 0.175m localization error (21% below dataset average) despite minimal visual texture, validating that uncertainty-aware fusion effectively prioritizes LiDAR geometric measurements when camera features are limited. Barriers achieve 82.2% mAP with marginally higher localization error (0.195m), consistent with elongated shape ambiguity in determining precise bounding box extent.

8. Robustness Evaluation

This section evaluates robustness under multiple sensor degradation scenarios relevant to real-world deployment.

submission. Results will be updated upon server restoration.

Table 10. Per-class performance on nuScenes validation set. Classes grouped by semantic category.

Class	mAP \uparrow	mATE \downarrow	mASE \downarrow	mAOE \downarrow	mAVE \downarrow	mAAE \downarrow
<i>Rigid Vehicles</i>						
Car	90.1	0.125	0.125	0.055	0.135	0.080
Truck	69.8	0.245	0.170	0.080	0.165	0.095
Bus	76.2	0.205	0.160	0.045	0.270	0.125
Trailer	49.3	0.350	0.190	0.620	0.125	0.070
Construction Vehicle	32.8	0.535	0.305	0.680	0.075	0.195
<i>Vulnerable Road Users</i>						
Pedestrian	93.4	0.095	0.245	0.195	0.120	0.060
Motorcycle	86.7	0.135	0.215	0.105	0.280	0.035
Bicycle	82.9	0.155	0.230	0.225	0.120	0.095
<i>Static Objects</i>						
Traffic Cone	85.6	0.175	0.295	N/A	N/A	N/A
Barrier	82.2	0.195	0.315	0.220	N/A	N/A
Overall	74.9	0.222	0.225	0.247	0.161	0.094

8.1. Calibration Robustness Analysis

Calibration drift occurs in deployed vehicles due to thermal expansion, vibration, and mounting stress [24]. To quantify robustness to extrinsic perturbations, synthetic rotational noise is applied to camera poses while maintaining fixed LiDAR coordinates. Figure 2 presents degradation curves across perturbation magnitudes.

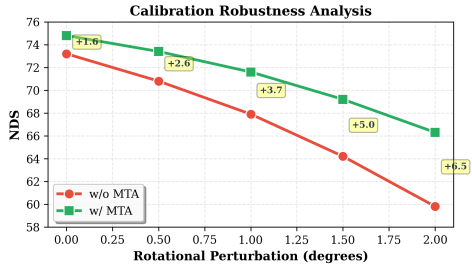


Figure 2. **Calibration robustness analysis.** Performance degradation under increasing rotational perturbation to camera extrinsics. The Multi-Modal Token Alignment (MTA) module provides increasing protection under larger calibration errors, reducing degradation by 52% at 2.0° perturbation (6.5 NDS improvement). At realistic 0.5° drift levels observed in field deployments [24], MTA maintains 98.1% of clean performance versus 96.7% without alignment. The divergence between the curves demonstrates that MTA’s benefits scale with the severity of the perturbation.

As shown in Figure 2, the Multi-Modal Token Alignment (MTA) module provides increasing protection under larger calibration errors. The gap between the two curves widens progressively from +1.6 NDS at clean conditions to +6.5 NDS at 2.0° perturbation, demonstrating that learned

token alignment becomes increasingly valuable as calibration degrades. These results validate that MTA effectively corrects residual calibration errors encountered during real-world operation.

8.2. Complete Sensor Dropout

Figure 3 evaluates performance under complete sensor failure scenarios, enabled by modality dropout training ($p_{\text{drop}} = 0.15$).

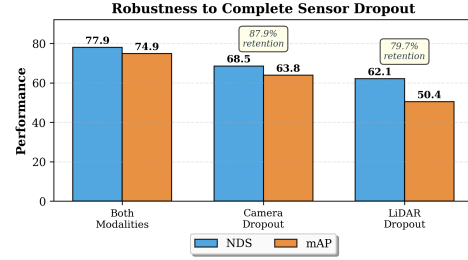


Figure 3. **Robustness to complete sensor dropout.** Under complete camera failure, the system retains 87.9% NDS and 85.2% mAP relative to the full-sensor baseline. Under complete LiDAR failure, retention drops to 79.7% NDS and 67.3% mAP. Although performance degrades significantly, the system remains functional, preserving essential safety margins required for fault-tolerant autonomous driving. The asymmetric degradation arises from complementary sensing roles: cameras provide rich semantic cues aiding coarse localization and recognition, whereas LiDAR contributes high-fidelity geometry necessary for precise 3D spatial reasoning.

Figure 3 reveals that the system maintains reasonable performance even under complete sensor failure. The retention percentages (87.9% for camera dropout vs. 79.7% for

LiDAR dropout) indicate asymmetric dependencies: camera features provide sufficient semantic and spatial information for coarse localization. At the same time, LiDAR geometry is more critical for precise 3D localization.

8.3. Performance Across Detection Range

Detection accuracy varies as a function of range due to sensor-specific degradation characteristics. Following the evaluation protocol in [35], we stratify performance by radial distance bins: 0–20m (near-field), 20–30m (mid-field), and beyond 30m (far-field, up to nuScenes’ 50m detection limit). Figure 4 presents results comparing BEVFusion LiDAR-only, BEVFusion, and MambaFusion across these intervals.

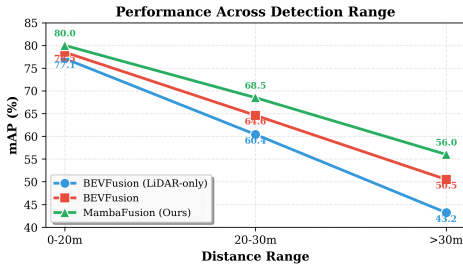


Figure 4. Performance across detection range on nuScenes validation set. Comparison of BEVFusion’s LiDAR-only backbone (blue), BEVFusion full fusion (red), and MambaFusion (ours). MambaFusion achieves consistent improvements with gains increasing at greater distances: +1.5 points at 0–20m, +3.9 points at 20–30m, and +5.5 points beyond 30m relative to BEVFusion. This pattern reflects complementary degradation profiles of camera and LiDAR sensors, with adaptive fusion providing the greatest benefits where sensor quality degrades most.

The range-dependent improvement pattern in Figure 4 validates the adaptive fusion mechanism’s effectiveness. Near-field performance (0–20m: 80.0 mAP) shows +1.5 point improvement over BEVFusion (78.5 mAP), where both sensors provide high-quality measurements. Mid-field performance (20–30m: 68.5 vs. 64.6 mAP) demonstrates larger gains of +3.9 points as LiDAR sparsity increases. Far-field performance (>30m: 56.0 vs 50.5 mAP) achieves +5.5 point improvement despite fundamental resolution limitations. The monotonically increasing improvement pattern (+1.5 → +3.9 → +5.5 points) demonstrates that adaptive fusion gates provide the greatest value where sensor degradation is most severe. BEVFusion’s own fusion gains over its LiDAR-only backbone (+1.4 → +4.2 → +7.3 points) show similar range-dependent patterns, confirming that multi-modal fusion benefits scale with single-sensor limitations.

8.4. Robustness to Sensor Corruptions (nuScenes-C)

The nuScenes-C benchmark [9] provides standardized evaluation across 20 corruption types spanning four categories: weather, sensor noise, motion blur, and object-level perturbations. Table 11 presents comprehensive results. MambaFusion achieves an average mAP of 68.5 under corruption with a RCE of 8.55

Performance Analysis and Specialization Patterns. MambaFusion achieves 68.5 mAP under corruption with 8.55% RCE, nearly matching RoboFusion’s [43] 8.58% while providing +4.6 mAP absolute improvement. This demonstrates effective robustness scaling: despite a higher clean baseline (74.9 vs. 69.91), corrupted performance ratios remain comparable (91.5

Performance patterns reveal clear specialization. **Sensor noise** represents the primary strength: spatial data loss (density, cutout, crosstalk) achieves 99.2–100% retention (+5.1 to +6.2 over RoboFusion), camera noise handling excels (+8.4 mAP average), and compensation benefits from learned alignment (+9.1 mAP, +21.7%). The MTA module and modality dropout training ($p_{drop} = 0.15$) successfully handle incomplete sensor coverage. Meanwhile, the validation of camera noise asymmetry (+8.4 vs +4.5 for LiDAR noise) suggests that geometric measurements substitute more effectively for degraded visual features than vice versa. **Motion blur** (73.8 mAP, +6.6 over RoboFusion) benefits from temporal SSMs [12] recovering sharp features across the 8-frame sequence. **Weather corruptions** show mixed results (average +0.5 over RoboFusion): strong on rain (+1.7), competitive on sunlight (+0.8) and fog (-0.5), but trailing on snow (-1.9) where bilateral degradation limits fusion benefits. **Object-level** corruptions demonstrate solid improvements (average +3.4 over RoboFusion), with local cutout and density benefiting from spatially-adaptive fusion.

Compared to BEVFusion [35] (+7.2 mAP) and TransFusion [1] (+9.7 mAP), MambaFusion demonstrates substantial robustness improvements. Results validate core architectural decisions—MTA alignment, modality dropout, uncertainty-aware gates, and temporal modeling—while revealing trade-offs: excellent performance is achieved when sensors remain operational despite data corruption, but modest gains are observed when bilateral physical degradation affects both modalities simultaneously.

Limitations. Snow corruption (-1.9 vs. RoboFusion) reveals limitations when atmospheric phenomena simultaneously degrade both modalities, suggesting that modality-agnostic decoding offers complementary advantages. LiDAR noise asymmetry reveals that visual features cannot

Table 11. Robustness evaluation on nuScenes-C validation set [9]. All values are mAP scores. Best result in **bold**, second best underlined. RCE = Relative Corruption Error. Baseline results from [43].

Corruptions	LiDAR-Only		Camera-Only			Camera-LiDAR Fusion			
	CenterPt [55]	PtPillars [22]	DETR3D [48]	BEVFormer [29]	FUTR3D [6]	TransFusion [1]	BEVFusion [35]	RoboFusion [43]	Ours
Clean	59.28	27.69	34.71	41.65	64.17	66.38	68.45	<u>69.91</u>	74.9
<i>Weather Corruptions</i>									
Snow	55.90	27.57	5.08	5.73	52.73	63.30	62.84	67.12	<u>65.2</u>
Rain	56.08	27.71	20.39	24.97	58.40	65.35	66.13	<u>67.58</u>	69.3
Fog	43.78	24.49	27.89	32.76	53.19	53.67	54.10	67.01	<u>66.5</u>
Strong Sunlight	54.20	23.71	34.66	41.68	57.70	55.14	64.42	<u>67.24</u>	68.0
<i>Sensor Noise Corruptions</i>									
Density	58.60	27.27	–	–	63.72	65.77	67.79	<u>69.48</u>	74.6
Cutout	56.28	24.14	–	–	62.25	63.66	66.18	<u>69.18</u>	74.3
Crosstalk	56.64	25.92	–	–	62.66	64.67	67.32	<u>68.68</u>	74.9
FOV Lost	20.84	8.87	–	–	26.32	24.63	27.17	<u>39.48</u>	46.0
Gaussian (L)	45.79	19.41	–	–	58.94	55.10	60.64	<u>57.77</u>	62.5
Uniform (L)	56.12	25.60	–	–	63.21	64.72	<u>66.81</u>	<u>64.57</u>	69.0
Impulse (L)	57.67	26.44	–	–	63.43	65.51	67.54	65.64	70.0
Gaussian (C)	–	–	14.86	15.04	54.96	64.52	64.44	<u>66.73</u>	74.6
Uniform (C)	–	–	21.49	23.00	57.61	65.26	<u>65.81</u>	65.77	74.2
Impulse (C)	–	–	14.32	13.99	55.16	64.37	64.30	<u>64.82</u>	73.8
Compensation	11.02	3.85	–	–	31.87	9.01	27.57	<u>41.88</u>	51.0
<i>Motion Corruptions</i>									
Motion Blur	–	–	11.06	19.79	55.99	64.39	64.74	<u>67.21</u>	73.8
<i>Object-Level Corruptions</i>									
Local Density	57.55	26.70	–	–	63.60	65.65	67.42	<u>66.74</u>	71.2
Local Cutout	48.36	17.97	–	–	61.85	63.33	63.41	<u>66.82</u>	70.8
Local Gaussian	51.13	25.93	–	–	62.94	63.76	64.34	<u>65.08</u>	69.5
Local Uniform	57.87	27.69	–	–	64.09	66.20	67.58	<u>66.71</u>	68.8
Local Impulse	58.49	27.67	–	–	64.02	66.29	67.91	<u>66.53</u>	68.3
Avg. (Corrupted)	49.78	22.99	18.71	22.12	56.88	58.77	61.35	<u>63.90</u>	68.5
RCE (%) ↓	16.01	16.95	46.07	46.89	11.34	11.45	10.36	<u>8.58</u>	8.55

adequately substitute for corrupted geometry. The FOV loss (46.0 mAP) demonstrates intrinsic limitations, as a 40

challenging nuScenes scenarios. The visualizations include bird’s-eye-view (BEV) representations with overlaid LiDAR point clouds and corresponding multi-camera panoramic views.

Figure 6 illustrates performance on a construction site scenario featuring large construction vehicles, barriers, and traffic cones. MambaFusion accurately detects and localizes construction equipment despite their substantial size and geometric complexity, while maintaining precise detection of small static objects (traffic cones) that exhibit minimal LiDAR returns. The BEV visualization demonstrates tight alignment between predicted and ground truth bounding boxes across objects at varying distances, validating the effectiveness of uncertainty-aware fusion in balancing camera semantic features with LiDAR geometric precision.

Figure 7 demonstrates performance on a dense urban intersection with multiple objects at various ranges. MambaFusion successfully detects most objects in this challenging scenario, accurately estimating their orientations and maintaining precise localization even for distant objects beyond 30m. However, several extremely occluded objects—where both camera and LiDAR measurements are severely degraded by full occlusion from foreground objects—are missed, representing inherent limitations when sensor visibility is completely blocked. The multi-camera

9. Computational Efficiency Analysis

9.1. Component-wise Latency Breakdown

Inference latency is profiled on an NVIDIA A100 GPU using 8-frame temporal sequences, a 900×1600 input resolution, and a 200×200 BEV discretization. Figure 5 decomposes total runtime by architectural component.

Figure 5 reveals that core encoding and fusion operations dominate computation, while proposed refinement modules add modest overhead. The pie chart (left) shows proportional distribution, confirming that no single component creates a bottleneck—the three largest components (LiDAR encoder, fusion decoder, camera encoder) contribute balanced shares (28.6%, 26.5%, 24.4%). The bar chart (right) provides absolute latencies, with refinement modules (GNN and GCD, highlighted with red borders) demonstrating that substantial accuracy gains (Table 3 in the main paper) come at a combined cost of only 12ms.

9.2. Qualitative Results

Figures 6 and 7 present representative qualitative results demonstrating MambaFusion’s detection performance on

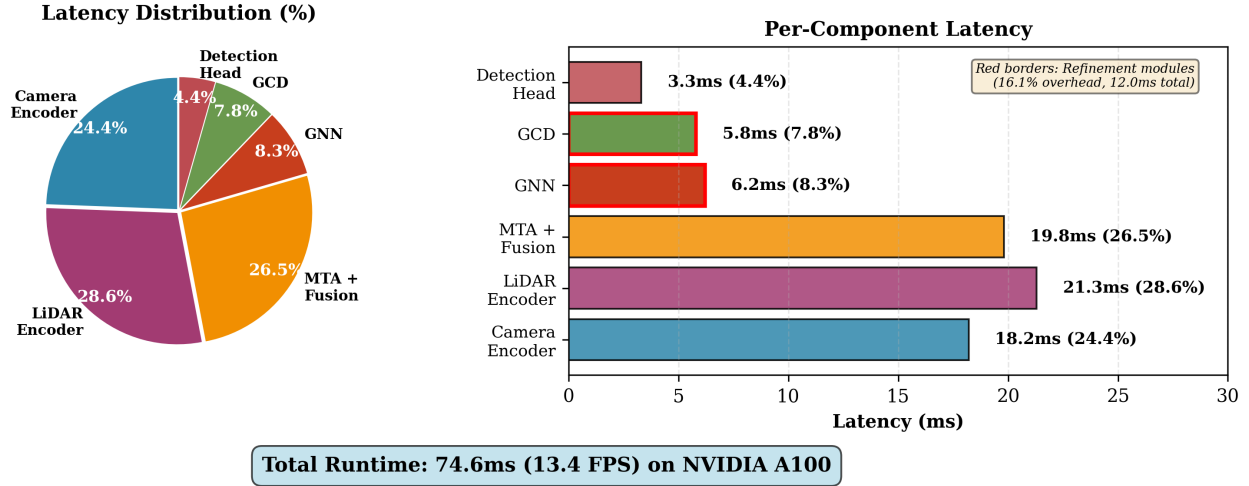


Figure 5. **Per-component latency breakdown on NVIDIA A100.** Left: Percentage distribution showing that the hybrid LiDAR encoder (28.6%) and fusion decoder with MTA (26.5%) constitute 55% of total latency. Right: Absolute latencies reveal that proposed refinement modules—GNN reasoning (6.2ms, red border) and geometry-conditioned diffusion (5.8ms, red border)—contribute only 16.1% combined overhead. Despite adding these refinement modules, the total runtime of 74.6ms (13.4 FPS) remains competitive due to linear-time Mamba blocks replacing quadratic temporal attention for BEV feature aggregation.

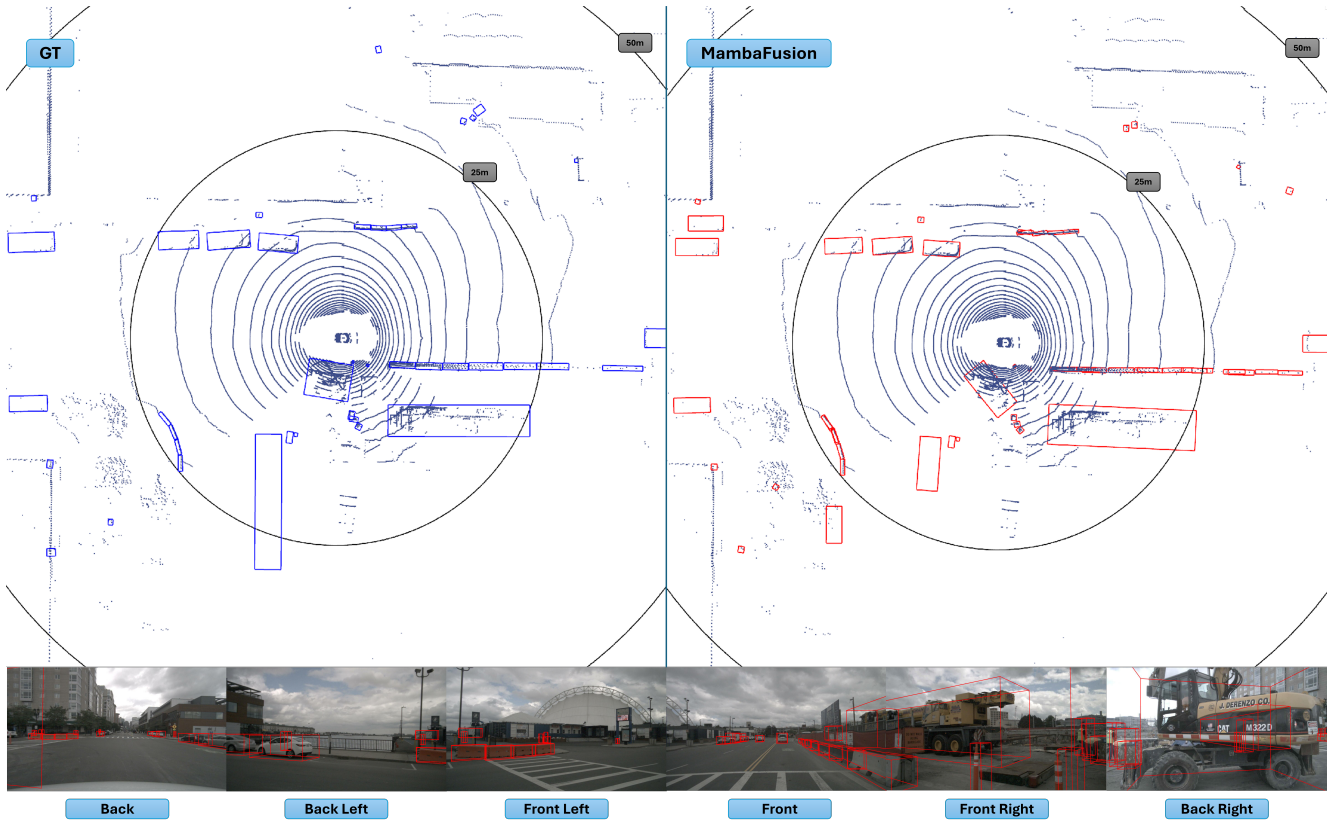


Figure 6. Qualitative results on construction site scenario from nuScenes validation set. Left: ground truth annotations (blue boxes). Right: MambaFusion predictions (red boxes). The scene contains construction vehicles, barriers, and traffic cones with varying distances and occlusion levels. MambaFusion accurately localizes large construction vehicles and maintains precise detection of small static objects (traffic cones, barriers) despite sparse LiDAR returns.

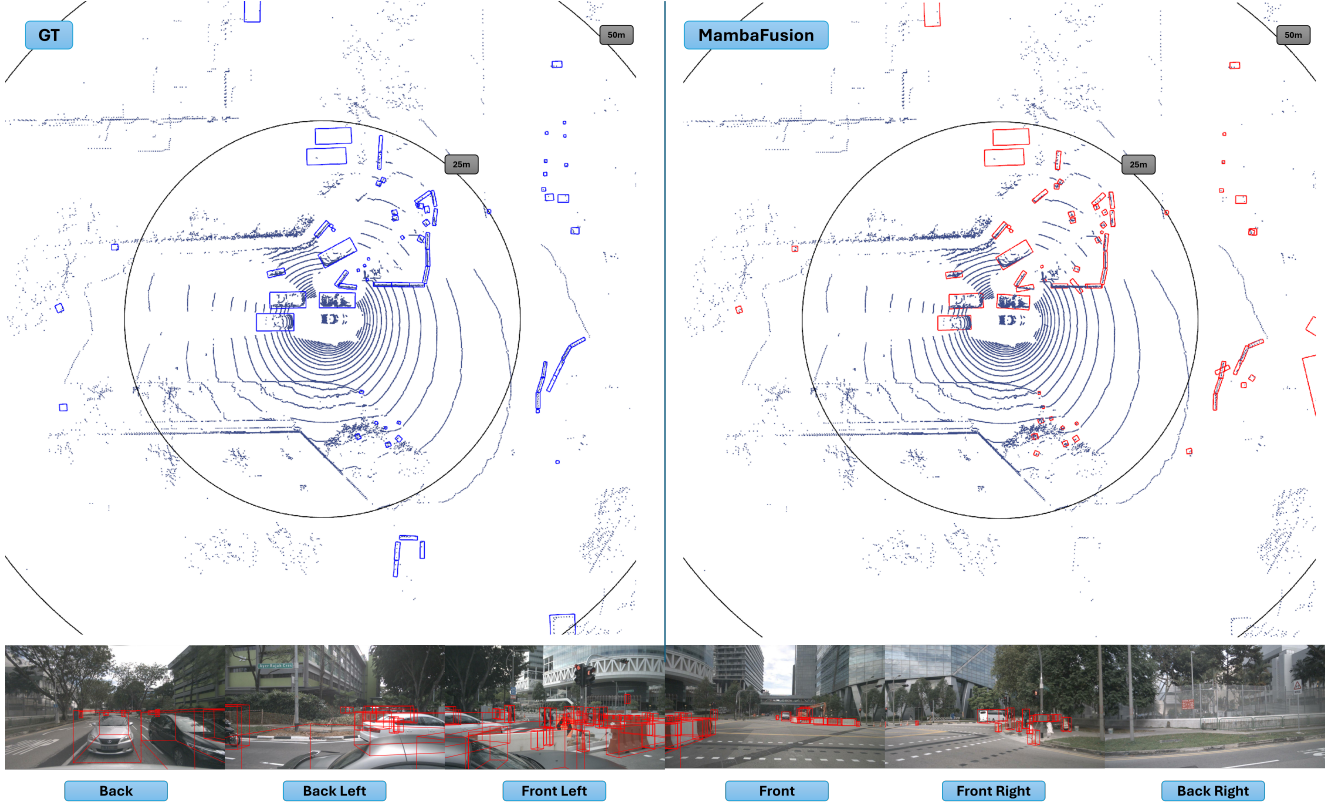


Figure 7. Qualitative results on dense urban intersection from nuScenes validation set. Left: ground truth annotations (blue boxes). Right: MambaFusion predictions (red boxes). The scene features multiple vehicles at various ranges in a complex intersection layout. MambaFusion detects most objects despite severe occlusions, accurately capturing vehicle orientations and maintaining localization precision in crowded scenarios.

views reveal that the method effectively handles moderate occlusions and challenging lighting conditions, maintaining detection consistency across different viewpoints. The spatial reasoning capability provided by the GNN module is evident in the accurate separation of closely spaced vehicles, where individual object identities are correctly preserved despite proximity.

These qualitative examples validate the quantitative improvements observed in Tables 1 and 10, demonstrating that MambaFusion achieves robust performance across diverse object categories, distance ranges, and scene complexities, while acknowledging remaining challenges in extreme occlusion scenarios where fundamental sensor limitations apply.